



# Hierarchical MAPSO-11 molecular sieves synthesized from aluminum isopropoxide: synergistic effect of acidity and morphology on the hydroisomerization of *n*-C<sub>16</sub>

Artur Malunov <sup>a</sup> , Dmitry Serebrennikov <sup>a</sup> , Roman Yakovenko <sup>b</sup> ,  
Nadezhda Filippova <sup>a\*</sup> , Svetlana Kostyleva <sup>a</sup> , Andrei Baryshev <sup>c</sup> , Marat Agliullin <sup>a</sup>

**a:** Institute of Petrochemistry and Catalysis , Ufa Federal Research Centre of the Russian Academy of Sciences, Ufa 450075, Russia

**b:** Platov South-Russian State Polytechnic University (NPI) , Novocherkassk 346428, Russia

**c:** Ufa Federal Research Centre of the Russian Academy of Sciences, Ufa 450054, Russia

\* Corresponding author: [filippova-ink@yandex.ru](mailto:filippova-ink@yandex.ru)

## Abstract

Bifunctional catalysts based on SAPO-11 molecular sieves exhibit high selectivity in the hydroisomerization of long-chain *n*-paraffins; however, their widespread application is constrained by moderate acidity and diffusion limitations within the 1D channels. Herein, we propose a strategy to enhance catalyst efficiency through the creation of a hierarchical structure and isomorphous substitution with magnesium (MAPSO-11). It was established that the use of aluminum isopropoxide promotes the formation of a hierarchical porous architecture composed of aggregated nanocrystals. The influence of magnesium on the morphology was elucidated: at an optimal MgO/Al<sub>2</sub>O<sub>3</sub> ratio of 0.1, primary crystals of minimal size (~50 nm) are formed, which ensures a maximized external surface area ( $S_{\text{EXT}} = 93 \text{ m}^2/\text{g}$ ) and secondary mesopore volume ( $V_{\text{meso}} = 0.19 \text{ cm}^3/\text{g}$ ). A further increase in magnesium content leads to crystal growth and a reduction in pore accessibility. TPD-NH<sub>3</sub> results confirm that the introduction of Mg significantly enhances the total acidity and the concentration of strong acid sites compared to conventional SAPO-11. Catalytic testing of Pt-containing systems in the hydroisomerization of *n*-hexadecane demonstrated that the developed mesoporosity and enhanced acidity enable a shift of the temperature window for maximum isomer yield to a lower temperature range (20–30 °C below that of SAPO-11). The obtained results demonstrate an effective approach for tuning the activity of hierarchical molecular sieves through precise control of the magnesium content, opening new avenues for the development of low-temperature catalysts for the production of low-pour-point oils and fuels.

## Key findings

- Hierarchical MAPSO-11 with intercrystalline mesoporosity was synthesized template-free using aluminum isopropoxide and a nanosized sol SiO<sub>2</sub>.
- The method formed 50–100 nm MAPSO-11 nanocrystals, reducing 1D diffusion channel lengths by 5–10 times.
- Optimal magnesium substitution (MgO/Al<sub>2</sub>O<sub>3</sub> = 0.1) synergistically increased strong Brønsted acid sites and external surface area.
- Pt/MAPSO-11(0.1) achieved an 82% C<sub>16</sub> isomer yield at 290 °C during *n*-hexadecane hydroisomerization, effectively suppressing hydrocracking.

© 2026, the Authors. This article is published in open access under the terms and conditions of the Creative Commons Attribution (CC BY) license (<http://creativecommons.org/licenses/by/4.0/>), which permits unrestricted reuse of the work in any medium provided the original work is properly cited.

## Accompanying information

### Article history

Received: 23.02.2026

Revised: 18.04.2026

Accepted: 21.04.2026

Available online: 21.04.2026

### Keywords

MAPSO-11 molecular sieves; hierarchical structure; aluminum isopropoxide; bifunctional catalysts; hydroisomerization of *n*-C<sub>16</sub>

### Funding

This research was funded by the Russian Science Foundation No. 23-73-10153.

### Supplementary information

Transparent peer review:

### Sustainable Development Goals



## 1. Introduction

Molecular sieves represent a cornerstone for the design of innovative catalytic systems and adsorption materials, owing to their unique textural and structural properties [1,2]. While conventional aluminosilicate zeolites have dominated industrial processes for decades, the last twenty years have been marked by a growing interest in aluminophosphate systems (AlPO<sub>4</sub>-n) and their isomorphously substituted derivatives (MeAPO-n, SAPO-n, MeAPSO-n). These materials combine extensive structural diversity with the ability for precise control of the nature and strength of acid sites, thereby opening new prospects for the design of catalysts tailored for specific chemical transformations [3–6].

According to the pioneering work of Wilson S.T. and co-workers (Union Carbide, 1984) [7], AlPO<sub>4</sub>-n and their derivatives belong to the class of zeolite-like microporous materials with pore sizes ranging from 3.8 Å (SAPO-18) to 12.7 Å (VPI-5) and diverse channel topologies, including one-dimensional (SAPO-11), two-dimensional (SAPO-40), and three-dimensional (SAPO-37) systems [7].

Among the large family of aluminophosphates, silicon-substituted analogues (SAPO-n) have gained the most significant practical importance. Large-scale industrial processes have already been implemented based on these materials: for instance, a catalyst based on SAPO-34 has been developed for the conversion of methanol to light olefins (MTO) [8], while SAPO-11 has found application in processes of isodewaxing of oils and diesel fractions [9]. Among these materials, the SAPO-11 molecular sieve (structure type AEL) is of particular interest due to the presence of a one-dimensional system of elliptical channels with dimensions of 4.0 × 6.5 Å and mild Brønsted acid sites (BAS). Catalysts based on molecular sieves with the AEL structure are recognized as among the most selective for the hydroisomerization of higher n-paraffins of the C<sub>7+</sub> fraction [10–15]. Furthermore, recent studies have demonstrated the versatility of SAPO-11-based catalysts in sustainable fuel production, including the hydroprocessing of waste plastic pyrolysis oils to lubricant base feedstocks [16], the one-step hydrodeoxygenation-isomerization of triglycerides to renewable diesel and aviation fuels [14,17,18]. However, it is worth noting that the BAS in conventional SAPO-11 exhibit a lower strength compared to 1D-10R aluminosilicate zeolites (ZSM-23, ZSM-48) [7,13,19–21]. This limitation necessitates conducting the hydroisomerization process at elevated temperatures, which leads to undesirable energy consumption and a reduction in the overall catalyst lifetime.

An effective strategy to overcome this limitation could involve the introduction of Mg into the crystal lattice of SAPO-n. It was previously shown [22] that the simultaneous isomorphous substitution of framework elements with Mg<sup>2+</sup> and Si<sup>4+</sup> ions (forming systems of the MAPSO-n type) allows for a dramatic modification of the acidic properties.

Using the SAPO-5 structure as an example, it was demonstrated that the introduction of magnesium provides an increase in the concentration of Brønsted acid sites by more than twofold – from 92 μmol/g (SAPO-5) to 230 μmol/g (MAPSO-5). This effect, arising from the coexistence of bridging ≡Mg-OH-P≡ and ≡Si-OH-Al≡ groups, leads to the formation of stronger acid sites. This not only enhances the overall activity in complex processes such as alkylation or hydroisomerization of paraffins but also enables achieving an optimal balance between feedstock conversion and selectivity towards target products.

A comparison of the catalytic properties of MgAPO-11 and SAPO-11 in the hydroisomerization of n-decane and n-dodecane [23–28] reveals the advantage of magnesium-containing systems in this process. It has been established that the formation of bridging Brønsted acid sites of the ≡Mg-OH-P≡ type provides a higher acid strength compared to the ≡Si-OH-Al≡ sites characteristic of SAPO-11. As a result, MgAPO-11 catalysts exhibit enhanced activity, enabling the maximum isomer yield to be achieved at significantly lower temperatures.

Thus, MAPSO-n type materials are highly promising for the development of bifunctional catalysts for the hydroisomerization of heavy n-paraffin fractions.

Another significant issue limiting the catalytic efficiency of materials with the AEL architecture (specifically, SAPO-11) is diffusion limitations arising from their one-dimensional microporous structure. Slow mass transfer of long-chain molecules within the micropores leads to a decrease in the rate of the main reaction and promotes undesirable secondary cracking side reactions.

To date, a number of approaches have been proposed for the targeted control of the morphology and the creation of hierarchical (micro-mesoporous) SAPO-11 structures [29–33]. However, the vast majority of known synthesis methods require the use of additional organic crystal growth modifiers (CGM) or secondary pore-forming templates (surfactants, polymers) [29–33]. Alternative approaches are also being actively developed, such as the dry gel conversion (DGC) method [34] and crystallization in two-phase systems [33].

These methods allow for effective control over the crystal size and morphology of SAPO-11; however, they have several significant drawbacks. These include the high cost of organic additives, the complexity of removing them (which requires high-temperature calcination), the risk of product contamination, and the need to dispose of toxic mother liquors. DGC and two-phase crystallization methods are often associated with challenges when scaling up, such as the use of volatile organic solvents and the necessity of additional purification steps. These challenges significantly limit their industrial implementation and increase the environmental burden.

In this context, the development of a simple, readily scalable, and environmentally benign method for the hydrothermal synthesis of nanoscale SAPO-11 without the

use of costly and difficult-to-dispose-of secondary organic modifiers remains a scientific and practical challenge.

Currently, there is a lack of information in the literature regarding methods for controlling the crystal morphology and forming a hierarchical (micro-mesoporous) structure for magnesium-containing MAPSO-11 systems.

We have previously shown [25,35–37] that the use of aluminum isopropoxide as an Al source and a highly reactive SiO<sub>2</sub> sol (particle size 1–4 nm) as a Si source enables the synthesis of hierarchical SAPO-11 without the use of costly crystal growth modifiers or surfactant-based mesoporegens. It was established that the nanosized SiO<sub>2</sub> sol plays a dual role at the initial stages of crystallization: it acts as a heteroatom that generates a negative lattice charge (necessary for the formation of BAS) and as a crystal growth modifier that promotes the formation of nanosized intergrowths. The application of this approach allows achieving a significantly higher concentration of acid sites compared to the use of commercial silicon precursors. However, the synthesis mechanisms of hierarchical MAPSO-11 systems, as well as the influence of magnesium content on their textural and catalytic properties in reactions involving long-chain C<sub>16+</sub> paraffins, remain unexplored.

Thus, the present work is devoted to the development of a scientifically grounded approach for the synthesis of MAPSO-11 molecular sieves with a hierarchical porous structure without the use of crystal growth modifiers and surfactants. Within the framework of the study, the influence of magnesium content on the crystal size, morphology, and acidic properties was investigated, which made it possible to identify the conditions for the formation of hierarchical nanosized intergrowths with high accessibility of BAS. The catalytic efficiency of the obtained materials was evaluated in the hydroisomerization of long-chain C<sub>16+</sub> paraffins. The presented results reveal new opportunities for the creation of energy-efficient catalysts based on molecular sieves with the AEL structure for the hydroisomerization of higher n-paraffins C<sub>16+</sub>, capable of providing a high yield of target isomers at reduced process temperatures.

## 2. Results

It is known the acidic properties of MeAlPO-n type molecular sieves directly depend on the amount and nature of

heteroatoms isomorphously incorporated into their crystal lattice [38,39]. In this regard, in the present study, a comparative analysis of the chemical composition of the initial reaction gels and the final crystallization products was carried out (Table 1).

The elemental analysis data show that the silicon and magnesium content in the synthesized SAPO-11 and MAPO-11 samples is lower than their initial concentration in the reaction gels. This is explained by kinetic and thermodynamic limitations during the incorporation of heteroatoms (Si, Mg) into the aluminophosphate framework in the course of crystallization, as a result of which some of the elements remain in the mother liquor.

A similar pattern is observed for the bimetallic MAPSO-11 systems: regardless of the initial MgO/Al<sub>2</sub>O<sub>3</sub> molar ratio, the degree of incorporation of magnesium and silicon into the solid phase turns out to be incomplete. Remarkably, the silicon content in the MAPSO-11 samples remains practically unchanged when varying the MgO/Al<sub>2</sub>O<sub>3</sub> ratio. This suggests that the presence of magnesium in the reaction medium during the crystallization stage does not exert a significant competitive influence on the process of silicon incorporation into the lattice.

To confirm the phase purity and evaluate the structural characteristics of the synthesized materials, X-ray diffraction analysis was carried out. Figure 1 shows the powder diffraction patterns of the obtained molecular sieves; for comparison, the diffractogram of pure AlPO<sub>4</sub>-11 synthesized under similar conditions is also provided.

The diffraction patterns of all the studied samples contain characteristic reflections corresponding to the AEL topology, indicating their high phase purity. Thus, it can be concluded that the use of aluminum isopropoxide as a precursor in combination with Si and Mg sources enables the successful formation of the target AEL structure. Moreover, the introduction of single heteroatoms (Si or Mg) leads to only a slight decrease in the crystallinity degree compared to the unmodified framework: all synthesized samples, with the exception of MAPSO-11(0.2), are highly crystalline (degree of crystallinity > 90%).

However, for the MAPSO-11 sample series, a clear trend towards a decrease in the crystallinity degree was revealed with an increase in the initial magnesium content in the gel (growth of the MgO/Al<sub>2</sub>O<sub>3</sub> ratio).

**Table 1** Phase and chemical composition of the synthesized molecular sieves with the AEL structure.

Sample	Chemical composition, Gel Al <sub>2</sub> O <sub>3</sub> •P <sub>2</sub> O <sub>5</sub> •MgO•SiO <sub>2</sub>	Chemical composition, AEL Al <sub>2</sub> O <sub>3</sub> •P <sub>2</sub> O <sub>5</sub> •MgO•SiO <sub>2</sub>	Phase	DC <sup>a</sup>
AlPO <sub>4</sub> -11	1.00:1.00:0.00:0.00	1.00:0.99:0.00:0.00	AEL	96
MAPO-11	1.00:1.00:0.10:0.00	1.00:1.00:0.07:0.00	AEL	95
SAPO-11	1.00:1.00:0.00:0.19	1.00:0.92:0.00:0.15	AEL	92
MAPSO-11(0.05)	1.00:1.00:0.05:0.20	1.00:0.92:0.04:0.16	AEL	91
MAPSO-11(0.1)	1.00:1.00:0.10:0.19	1.00:0.92:0.08:0.15	AEL	91
MAPSO-11(0.2)	1.00:1.00:0.19:0.20	1.00:0.92:0.14:0.15	AEL	85

<sup>a</sup> DC is the degree of crystallinity, %

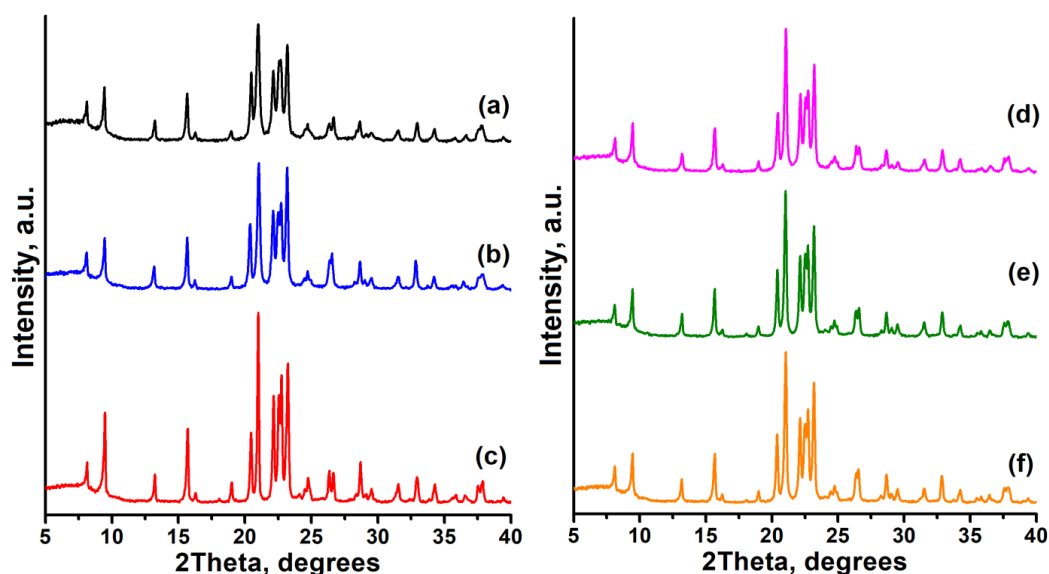


**Figure 1** XRD patterns of crystalline molecular sieves with the AEL structure: (a)  $\text{AlPO}_4$ -11 sample; (b) MAPO-11 sample; (c) SAPO-11 sample; (d) MAPSO-11(0.05) sample; (e) MAPSO-11(0.10) sample; (f) MAPSO-11(0.20) sample.

This effect is due to the mechanism of isomorphous substitution: the incorporation of magnesium ( $\text{Mg}^{2+}$ ) into the aluminum ( $\text{Al}^{3+}$ ) positions of the aluminophosphate framework inevitably causes local lattice distortions and the generation of structural defects.

An increase in the magnesium concentration at the stages of nucleation and crystal growth leads to the accumulation of such defects in the framework, which contributes to partial amorphization of the material. Thus, upon reaching the maximum studied  $\text{MgO}/\text{Al}_2\text{O}_3$  ratio of 0.2, the crystallinity of the target product did not exceed 85%

Figure 2 presents SEM images of the synthesized molecular sieve samples with the AEL structure, differing in chemical composition. As can be seen from the presented

micrographs, all samples consist of spherical aggregates (intergrowths) ranging in size from 2 to 3  $\mu\text{m}$ . Moreover, variation in the chemical composition leads to changes not only in the size of the aggregates themselves but also in the morphology and dimensions of the primary crystals that form them.

Thus, the  $\text{AlPO}_4$ -11 sample is formed by spherical aggregates ( $\sim 1$ –2  $\mu\text{m}$ ) consisting of primary crystals in the form of elongated prisms (100–500 nm). The introduction of magnesium into the aluminophosphate lattice (MAPO-11 sample) does not cause significant changes in the size of the secondary structures, nor in the morphology of the primary crystals: similar elongated prisms with sizes ranging from 100 to 500 nm are observed for this sample.

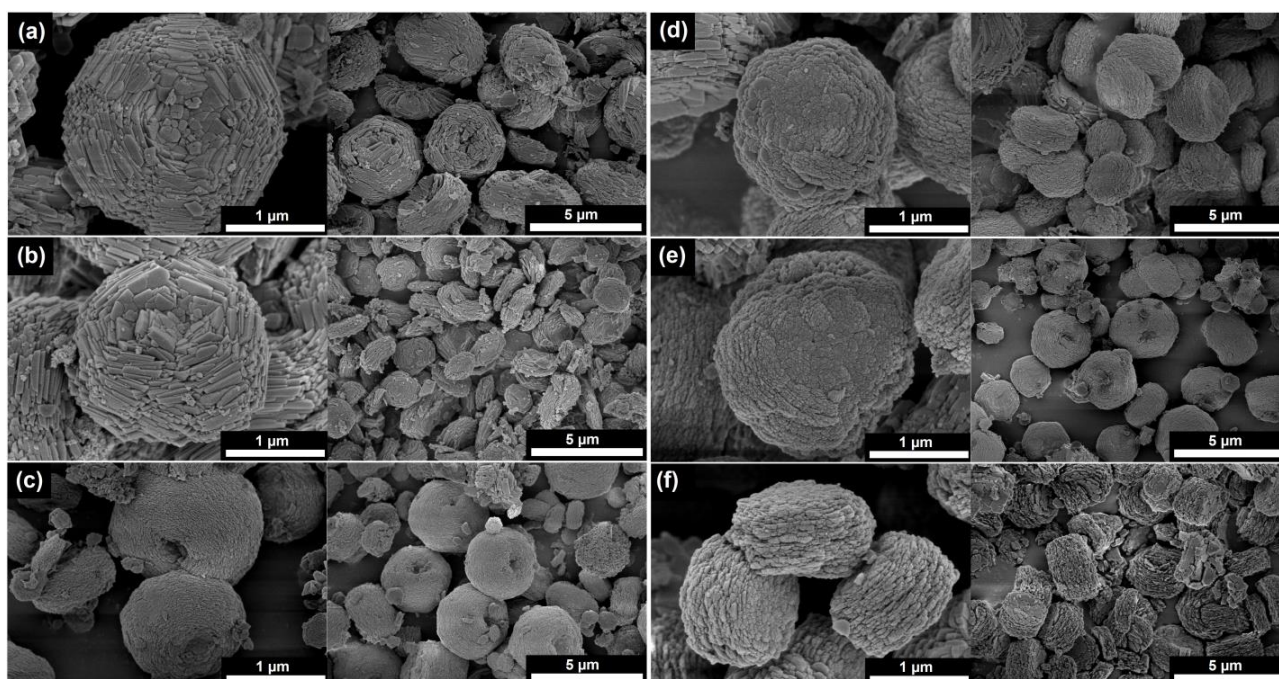


**Figure 2** SEM images of the samples: (a)  $\text{AlPO}_4$ -11 sample; (b) MAPO-11 sample; (c) SAPO-11 sample; (d) MAPSO-11(0.05) sample; (e) MAPSO-11(0.10) sample; (f) MAPSO-11(0.20) sample.

In contrast, the introduction of silicon leads to notable structural transformations. The SAPO-11 sample is characterized by the formation of larger spheroidal aggregates (2–3  $\mu\text{m}$ ) composed of nanocrystals in the form of thin plates and cubes with sizes of 50–100 nm, which form the hierarchical structure. As we have previously shown [25,35–37], the formation of hierarchical SAPO-11 is due to the use of aluminum isopropoxide and a highly reactive  $\text{SiO}_2$  sol with a particle size of 1–3 nm. This sol inhibits crystal growth, which makes it possible to obtain nanocrystalline materials without the use of additional organic growth modifiers.

The incorporation of magnesium into the silicoaluminophosphate lattice at a  $\text{MgO}/\text{Al}_2\text{O}_3$  molar ratio of 0.05 in the reaction gel does not lead to a noticeable change in morphology. The MAPSO-11(0.05) sample consists of aggregates comparable in size to SAPO-11, formed by nanocrystals with a size of  $\sim 50$  nm. However, a further increase in the magnesium content ( $\text{MgO}/\text{Al}_2\text{O}_3 = 0.10$ ) promotes the coarsening of primary crystals to 50–100 nm while preserving their shape (cubes and plates). Finally, for the MAPSO-11(0.2) sample with the maximum magnesium content, aggregates similar in size to MAPSO-11(0.05) and MAPSO-11(0.1) are observed, but formed from significantly larger primary crystals (100–200 nm) having the shape of elongated prisms.

It should be emphasized that for molecular sieves with the AEL structure, possessing a one-dimensional channel system, preferential crystal growth in the [001] direction is typical. In this case, the pore mouths can be located on

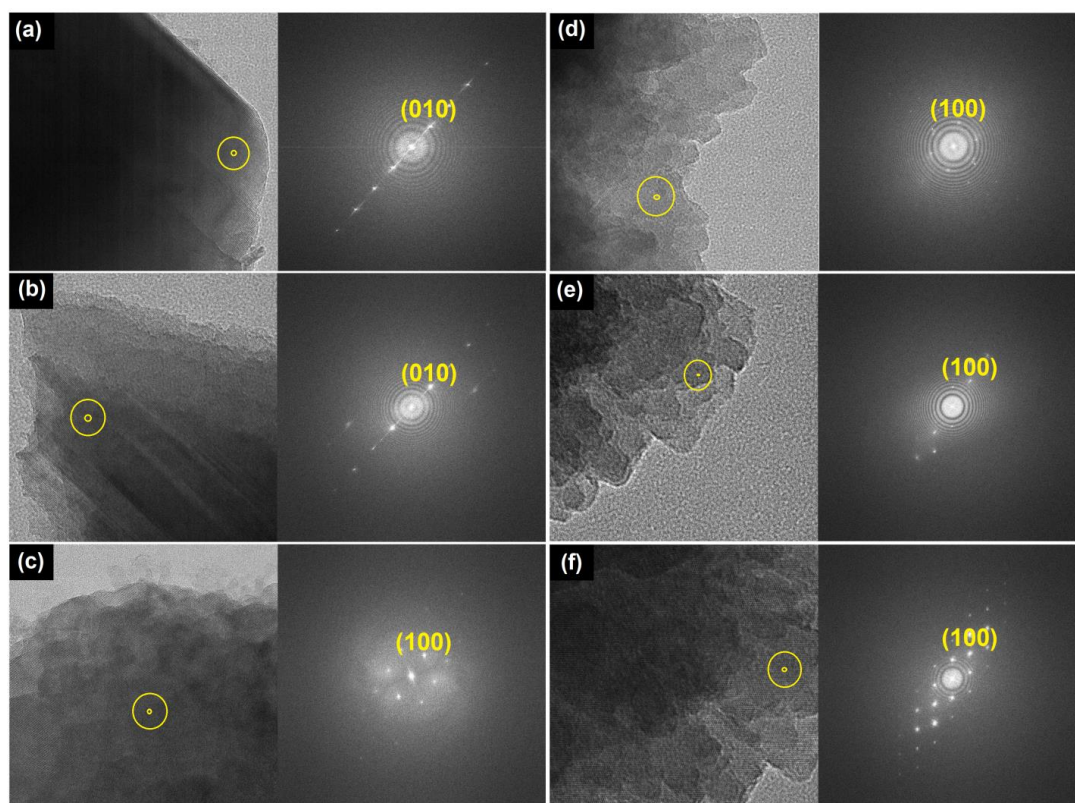
different crystallographic facets depending on the synthesis conditions. This feature often leads to the formation of crystals with a high aspect ratio, which creates prerequisites for the emergence of additional diffusion limitations. In this regard, for one-dimensional channel zeolite-like materials, it is critically important to establish the crystallographic orientation of the facets: the determining influence on molecular diffusion is exerted not only by the absolute size of the crystals but also by their morphology, on which the spatial accessibility of the pore mouths depends.

Figure 3 presents TEM images and Fast Fourier Transform (FFT) patterns for the synthesized series of molecular sieves.

According to the TEM data, the crystals of unmodified aluminophosphate  $\text{AlPO}_4$ -11 have the shape of elongated prisms with a length of  $\sim 200$ – $300$  nm, which is in good agreement with the SEM results (Figure 2).

The FFT pattern for the selected region corresponds to diffraction from a single crystal with an interplanar spacing  $d = 0.942$  nm, which is close to the theoretical value for the (010) plane ( $d = 0.935$  nm).

Consequently, in  $\text{AlPO}_4$ -11 crystals, the one-dimensional 10-membered ring (10R) channels open onto the end surfaces (tips) of the elongated prism. For the MAPO-11 sample, similar results were obtained, confirming the localization of the 1D-10R channel mouths at the prism tips. In turn, analysis of TEM images (Figure 3) of individual flat and cubic nanocrystals on the periphery of the aggregate of the SAPO-11 sample revealed an interplanar spacing  $d = 1.32$  nm.



**Figure 3** TEM images and SAED patterns of molecular sieve samples with the AEL structure: (a)  $\text{AlPO}_4$ -11 sample; (b) MAPO-11 sample; (c) SAPO-11 sample; (d) MAPSO-11(0.05) sample; (e) MAPSO-11(0.10) sample; (f) MAPSO-11(0.20) sample.

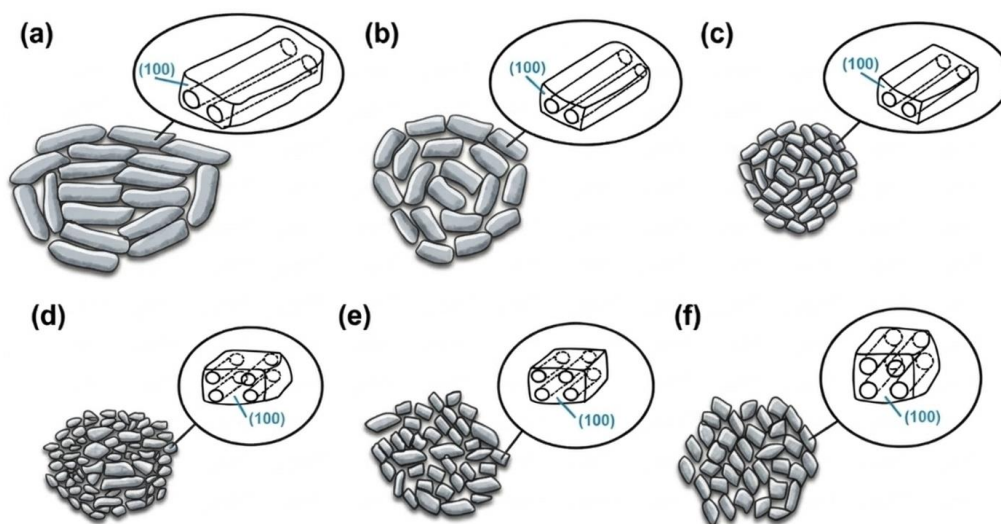


**Figure 4** Schematic representation of the localization of 1D-10R channels within the crystal volume of molecular sieve samples with the AEL structure: (a)  $\text{AlPO}_4\text{-11}$  sample; (b) MAPO-11 sample; (c) SAPO-11 sample; (d) MAPSO-11(0.05) sample; (e) MAPSO-11(0.10) sample; (f) MAPSO-11(0.20) sample.

The proximity of this value to  $d = 1.34$  nm for the (100) plane suggests that, in this case, the one-dimensional channels are localized on the broad surfaces (facets) of the plates and cubes. A similar pattern is observed for MAPSO-11(0.05), where the 1D-10R channels also open onto the surface of the platy and cubic nanocrystals.

For the MAPSO-11(0.1) sample, a diffraction pattern with an interplanar spacing  $d = 0.942$  nm ((010) plane) is recorded at the edge of the aggregate. This indicates that the 1D-10R channels are once again oriented along the long axis of the prism. For the MAPSO-11(0.2) sample, even more elongated prisms with a similar interplanar spacing  $d = 0.942$  nm ((010) plane) are observed, indicating the localization of the 1D-10R channel mouths at the prism tips, as in the case of MAPSO-11(0.1).

Figure 4 presents simplified schematic diagrams of the morphology of the synthesized molecular sieves with the AEL structure, based on the results of a comprehensive analysis of SEM and TEM data (including SAED/FFT diffraction). These schemes clearly illustrate the different spatial localization of the one-dimensional channels relative to the external surface of the crystals.

A comparison of the average crystal sizes of the aluminophosphate group ( $\text{AlPO}_4\text{-11}$  and MAPO-11) with their silicon-containing analogues (SAPO-11 and MAPSO-11) reveals significant structural differences. It becomes evident that the actual length of the one-dimensional 10-membered ring (10R) channels in the nanosized samples (SAPO-11 and MAPSO-11) is approximately 5–10 times smaller than in the macrocrystalline samples ( $\text{AlPO}_4\text{-11}$  and MAPO-11). Such a substantial reduction in the diffusion path length suggests a significant improvement in intrachannel mass transfer, as well as an increase in the spatial accessibility of the internal acid sites for reactant molecules.

Textural characteristics of the synthesized samples were analyzed by low-temperature nitrogen adsorption-

desorption. Figure 5 shows the corresponding isotherms and pore size distribution curves, while Table 2 summarizes the porous structure parameters.

For all studied samples, type IV isotherms according to the IUPAC classification with a pronounced hysteresis loop are observed, which is a characteristic feature of micro-mesoporous materials. The broad pore size distribution in the range from 2 to 30 nm confirms the formation of a developed mesopore system.

From the obtained results, it can be seen that the silicon-containing molecular sieves are characterized by a larger mesopore volume ( $V_{\text{meso}}$ ) and external specific surface area ( $S_{\text{EXT}}$ ) compared to the aluminophosphates  $\text{AlPO}_4\text{-11}$  and MAPO-11. This is due to the fact that the structure of these Si-containing materials is composed of nanocrystals of minimal size (50–100 nm). The void space between these nanoparticles forms intercrystalline mesoporosity, and the small size of the primary crystals provides a developed external surface.

For the MAPSO-11 series, increasing the magnesium content in the reaction gel leads to a regular decrease in mesopore volume and external surface area. As shown by SEM and TEM, this effect is directly related to the coarsening of primary crystals. Specifically, the crystals transition from nanoscale to larger forms. Thus, the MAPSO-11(0.05) sample, consisting of the smallest nanocrystals (~50 nm), possesses the maximum values of specific surface area and mesopore volume in this series.

It is important to emphasize that the key role in the formation of such a hierarchical micro-mesoporous structure is played by the high reactivity of the aluminum precursor (aluminum isopropoxide) and the use of nanosized  $\text{SiO}_2$  sol. It is their application that promotes rapid nucleation and the formation of primary nanocrystals, whereas the use of conventional boehmite or coarse silicon sources typically leads to the formation of large micron-sized or submicron crystals [40–43].

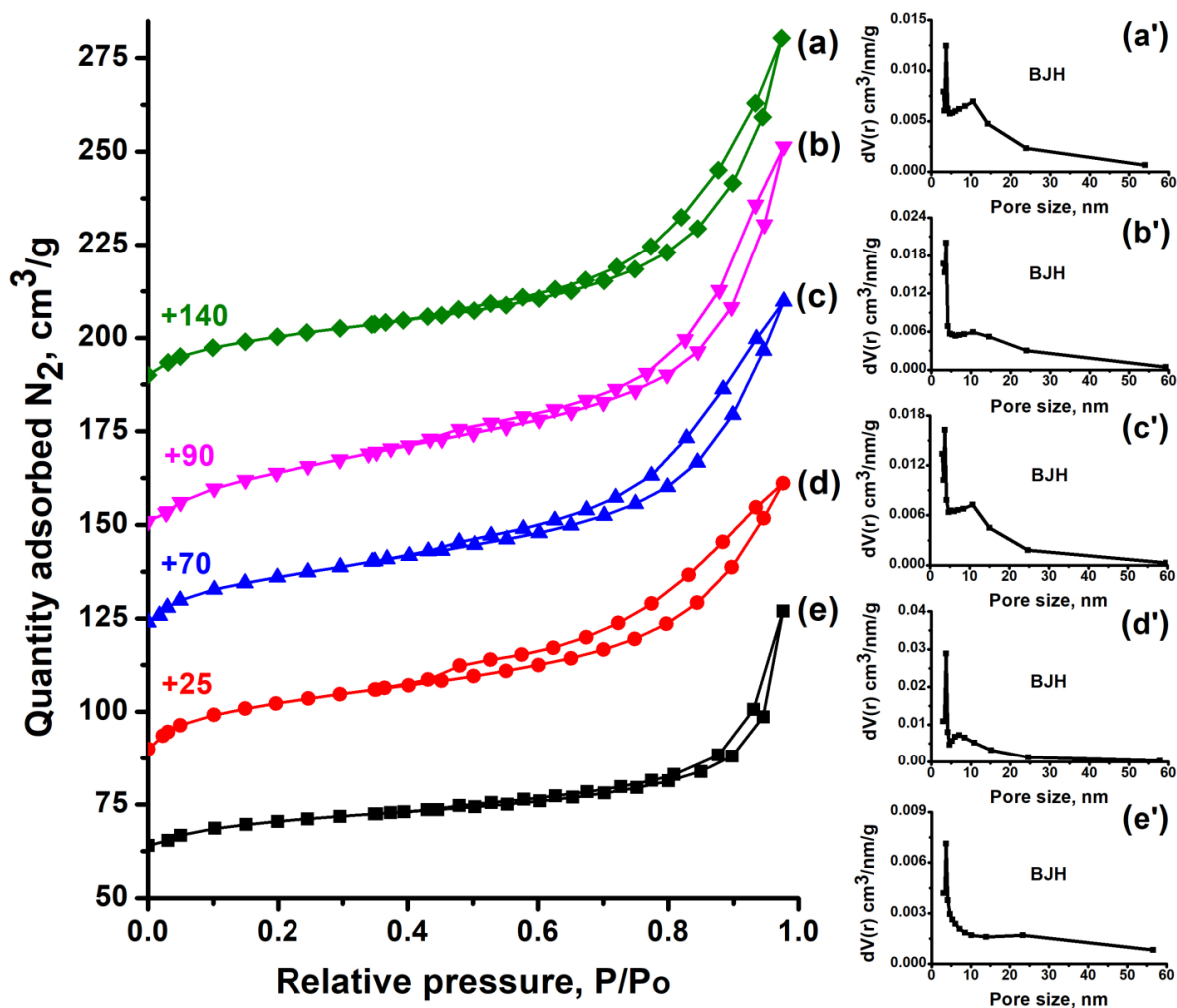


**Figure 5** Nitrogen adsorption-desorption isotherms and pore size distributions for molecular sieve samples with the AEL structure: (a, a') MAPO-11 sample; (b, b') SAPO-11 sample; (c, c') MAPSO-11(0.05) sample; (d, d') MAPSO-11(0.10) sample; (e, e') MAPSO-11(0.20) sample.

**Table 2** Porous structure parameters of the synthesized molecular sieve samples with the AEL structure.

Sample	$S_{\text{BET}}$ , $\text{m}^2/\text{g}$	$S_{\text{EXT}}$ , $\text{m}^2/\text{g}$	$V_{\text{micro}}$ , $\text{cm}^3/\text{g}$	$V_{\text{meso}}$ , $\text{cm}^3/\text{g}$
AlPO <sub>4</sub> -11	209	32	0.09	0.15
MAPO-11	231	49	0.08	0.11
SAPO-11	264	68	0.07	0.14
MAPSO-11(0.05)	228	73	0.07	0.15
MAPSO-11(0.10)	264	93	0.07	0.19
MAPSO-11(0.20)	204	61	0.05	0.16

$S_{\text{BET}}$  is the specific surface according to BET;  $S_{\text{EXT}}$  is the external specific surface area;  $V_{\text{micro}}$  is the specific volume of micropores;  $V_{\text{meso}}$  is the specific volume of mesopores

Thus, the results of the study demonstrate that the simultaneous use of highly reactive aluminum and silicon precursors represents an effective approach to the synthesis of hierarchical molecular sieves. Moreover, varying the initial MgO/Al<sub>2</sub>O<sub>3</sub> molar ratio serves as a convenient additional tool for fine-tuning the textural properties and porous structure parameters of the target catalysts.

It is known that the strength and concentration of Brønsted acid sites (BAS) in SAPO-*n* molecular sieves directly depend on the mechanism of silicon incorporation (substitution) into the aluminophosphate lattice [3]. For

SAPO-*n*, two main mechanisms are generally accepted: SM2, which involves the isolated substitution of P<sup>5+</sup> by Si<sup>4+</sup> with the formation of a Si(4Al) environment, and SM3, in which pairs of Al<sup>3+</sup>-P<sup>5+</sup> are replaced by 2 Si<sup>4+</sup>, leading to the formation of "silicate islands" with Si(*n*Si, (4-*n*)Al) environments. The SM2 mechanism leads to the formation of the maximum number of BAS. In the case of the formation of silicate islands (SM2+SM3 mechanism), BAS are generated only at their boundary with the aluminophosphate matrix, and these acid sites are presumed to possess greater strength [3,44].

To investigate the mechanisms of silicon incorporation in the synthesized MeAPO-11 samples, <sup>29</sup>Si MAS NMR spectroscopy was employed. Figure 6 presents the spectra, and Table 3 summarizes the results of their deconvolution. The spectra of all samples represent a broad resonance signal (from -80 to -120 ppm), which was deconvoluted into six Gaussian components. The signals at -91, -97, -102, -106, and -112 ppm were assigned to silicon atoms in Si(4Al), Si(3Al, 1Si), Si(2Al, 2Si), Si(1Al, 3Si), and Si(4Si, 0Al) environments, respectively, while the signal at -85 ppm is associated with amorphous aluminosilicate fragments [31,45-47].

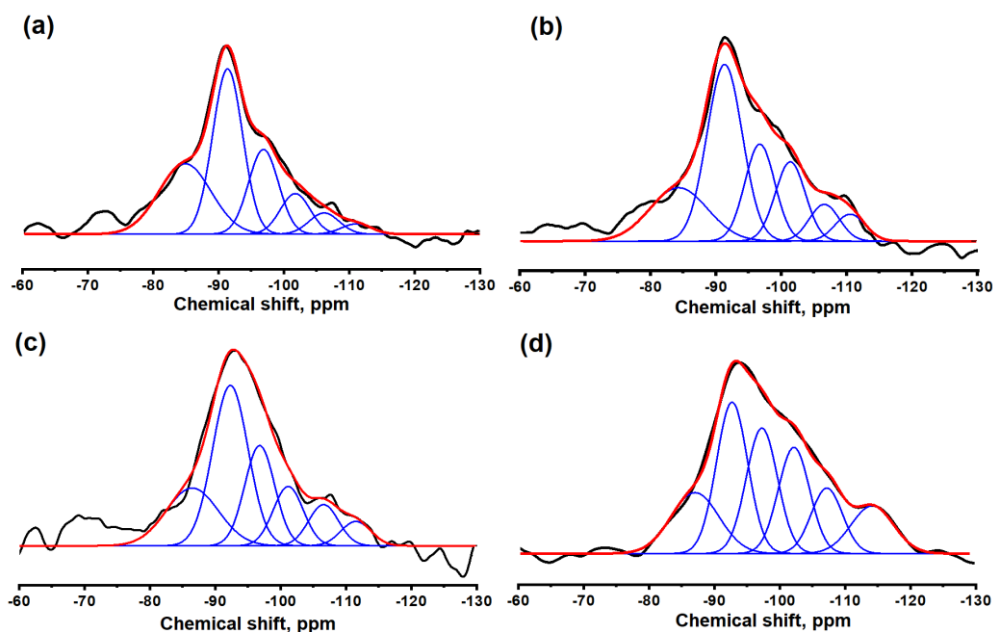


**Figure 6**  $^{29}\text{Si}$  MAS NMR spectra of Si-containing molecular sieve samples with the AEL structure: (a) SAPO-11 sample; (b) MAPSO-11(0.05) sample; (c) MAPSO-11(0.1) sample; (d) MAPSO-11(0.2) sample.

**Table 3** Deconvolution results of the  $^{29}\text{Si}$  MAS NMR spectra for Si-containing molecular sieve samples with the AEL structure

Sample	Deconvolution, (%)					
	-85 ppm	Si (0Si, 4Al) -91 ppm	Si (1Si, 3Al) -97 ppm	Si (2Si, 2Al) -102 ppm	Si (3Si, 1Al), -107 ppm	Si (4Si, 0Al), -112 ppm
SAPO-11	27	37	19	9	6	2
MAPSO -11(0.05)	19	37	19	11	9	5
MAPSO -11(0.1)	18	38	17	14	8	5
MAPSO -11(0.2)	15	25	20	17	12	11

For the SAPO-11, MAPSO-11(0.05), and MAPSO-11(0.1) samples, signals in the range of -85 to -102 ppm predominate. This indicates primarily isolated incorporation of silicon into the crystal lattice. In contrast, the MAPSO-11(0.2) sample shows signals mainly in the region of -106 to -112 ppm, evidencing the prevalence of silicon in the form of silicate islands. This means that an increase in the magnesium content in the lattice leads to a change in the mechanism of silicon incorporation into the framework, and upon reaching a certain threshold concentration, it begins to hinder the isolated incorporation of silicon. This trend is explained by the fact that the incorporation of magnesium heteroatoms into the aluminophosphate framework is competitive in nature with respect to silicon and is strictly controlled by thermodynamic and electrostatic factors, which prevents further isolated incorporation of silicon. It is important to note that with an increase in the magnesium content, no decrease in the silicon content is observed; rather, the mechanism of its incorporation predominantly changes.

The key characteristics of molecular sieves with the AEL structure that determine their catalytic activity are the nature and concentration of acid sites, as well as the specific one-dimensional pore system. The acidic properties of the synthesized molecular sieve samples were studied by temperature-programmed desorption of ammonia and IR spectroscopy of adsorbed pyridine (Figure 7, Table 4). The obtained desorption profiles for all investigated

materials are characterized by the presence of three broad regions corresponding to the removal of ammonia from acid sites of varying strength. The desorption peak maxima observed in the temperature regions around 200, 300, and 400 °C were assigned to weak, medium, and strong acid sites, respectively.

The total content of acid sites varies significantly depending on the elemental composition of the framework.

The lowest value of the total acid site concentration is characteristic of the MAPO-11 sample. The SAPO-11 sample with a fixed  $\text{SiO}_2/\text{Al}_2\text{O}_3$  molar ratio demonstrates a higher total acid site content. Further simultaneous incorporation of magnesium in the MAPSO-11 series samples, with a fixed silicon content and varying magnesium amounts, promotes an even more substantial increase in the total acid site concentration. The maximum value of the total acid site content is observed for the MAPSO-11 sample with an  $\text{MgO}/\text{Al}_2\text{O}_3$  molar ratio of 0.05, whereas the samples with ratios of 0.1 and 0.2 demonstrate somewhat lower total acid site concentrations.

The formation of acid sites in the studied materials occurs as a result of the incorporation of silicon and magnesium atoms into the aluminophosphate crystal lattice. Upon isomorphous substitution of phosphorus atoms by silicon and aluminum atoms by magnesium, a local charge imbalance arises, which is compensated by protons that act as Brønsted acid sites. In the MAPO-11 sample, acid sites are formed exclusively due to the incorporation of

magnesium. In the SAPO-11 sample, acidity is caused by the substitution of phosphorus atoms by silicon. In the MAPSO-11 sample series, the silicon content is fixed at a  $\text{SiO}_2/\text{Al}_2\text{O}_3$  ratio of 0.2, while the amount of magnesium varies from 0.05 to 0.2 in terms of the  $\text{MgO}/\text{Al}_2\text{O}_3$  molar ratio. The higher acid site content in the MAPSO-11 samples compared to MAPO-11 and SAPO-11 is explained by the simultaneous presence of both types of substitution, which leads to an additive effect in the formation of acid sites.

The MAPSO-11(0.05) sample demonstrates the maximum total amount of acid sites, which may indicate that the limit for magnesium incorporation into the crystal lattice has been reached. In the case of the MAPSO-11 sample with an  $\text{MgO}/\text{Al}_2\text{O}_3$  molar ratio of 0.2, a limitation on the incorporation of magnesium into the framework structure is probably observed. Excess magnesium is incorporated into the crystal lattice less efficiently during the synthesis process, which may lead to the formation of extra-framework magnesium species or secondary phases that do not contribute to the acidity of the material. This explains the slight decrease in the total acid site content for the sample with the highest magnesium content ( $\text{MgO}/\text{Al}_2\text{O}_3 = 0.2$ ) compared to the samples with a lower  $\text{MgO}/\text{Al}_2\text{O}_3$  ratio.

The distribution of acid sites by strength also exhibits a dependence on the sample composition. The SAPO-11 sample possesses the lowest concentration of strong acid sites, whereas the introduction of magnesium into the MAPO-11 structure leads to an increase in the number of strong sites. The highest values of strong acid site concentration are achieved for the MAPSO-11 series samples with an  $\text{MgO}/\text{Al}_2\text{O}_3$  molar ratio of 0.1. The strength of the acid sites, estimated from the temperature of the ammonia desorption peak maximum, correlates with the data on the concentration of strong acid sites. The lowest desorption temperature is characteristic of the SAPO-11 sample (378 °C), while the maximum value is observed for the MAPSO-11(0.1) sample (397 °C). The obtained results are consistent with literature data indicating that the substitution of aluminum atoms by magnesium leads to the formation of stronger acid sites compared to the substitution of phosphorus atoms by silicon [24,48], which is due to differences in ionic radii and electronegativity. Magnesium fits better into the framework structure, providing greater polarizability of the oxygen bonds and flexibility of the T-OH-T angles.

To distinguish between different types of acid sites, the acidic properties of the molecular sieves were investigated by FTIR spectroscopy of adsorbed pyridine. The spectra exhibit absorption bands corresponding to pyridine interacting with Brønsted and Lewis acid sites [49]. Bands at 1638 and 1546  $\text{cm}^{-1}$  are attributed to pyridinium ions, confirming the presence of Brønsted acid sites (BAS), while bands in the regions of 1612–1623 and 1449–1454  $\text{cm}^{-1}$  correspond to pyridine coordinatively bonded to Lewis acid sites (LAS). A band at 1490  $\text{cm}^{-1}$ , arising from contributions of both BAS and LAS, is observed in all samples. The precise positions of the LAS-related bands depend on the composition: for the Mg-containing MAPO-11 sample, they appear at 1612 and 1449  $\text{cm}^{-1}$ ; for the Si-containing SAPO-11 sample, they shift to 1623 and 1454  $\text{cm}^{-1}$ ; and for MAPSO-11 series, a composite pattern with bands at 1623, 1615, and 1451  $\text{cm}^{-1}$  is recorded, reflecting the simultaneous presence of both substitution types.

The lowest BAS concentration is observed for the purely Mg-substituted MAPO-11 sample (49  $\mu\text{mol/g}$ ), whereas the introduction of silicon in SAPO-11 raises this value to 91  $\mu\text{mol/g}$ . Co-substitution in the MAPSO-11 series further enhances Brønsted acidity, reaching a maximum of 109  $\mu\text{mol/g}$  for the sample with an  $\text{MgO}/\text{Al}_2\text{O}_3$  ratio of 0.05. At higher magnesium loadings, the BAS concentration gradually decreases to 106  $\mu\text{mol/g}$  for MAPSO-11(0.2) and 99  $\mu\text{mol/g}$  for MAPSO-11(0.1), which aligns with the proposed limit of efficient magnesium incorporation into the framework. SAPO-11 exhibits the lowest LAS concentration (19  $\mu\text{mol/g}$ ), which increases across the MAPSO-11 series to 28, 40, and 63  $\mu\text{mol/g}$  for  $\text{MgO}/\text{Al}_2\text{O}_3$  ratios of 0.05, 0.1, and 0.2, respectively. The purely magnesium-containing MAPO-11 sample shows the highest LAS concentration (64  $\mu\text{mol/g}$ ).

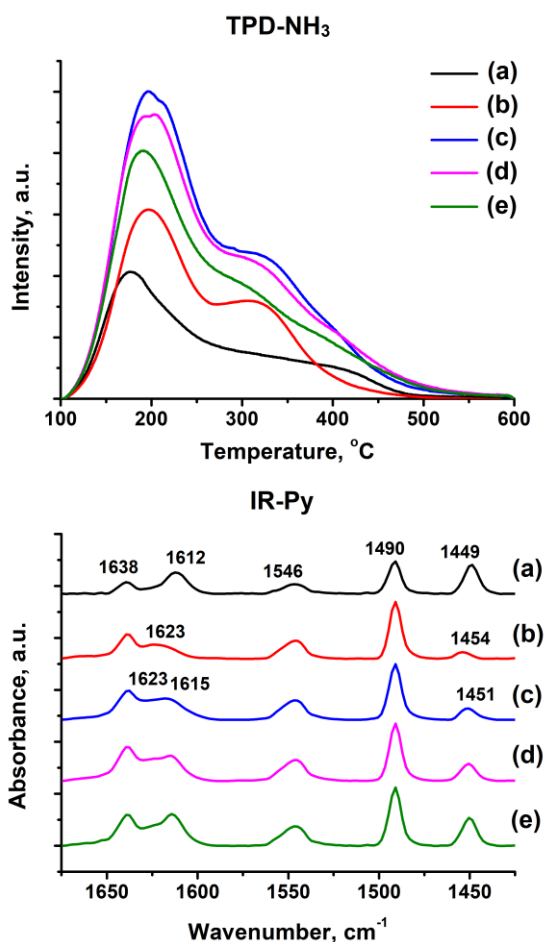


**Figure 7** Temperature-programmed desorption of ammonia (TPD- $\text{NH}_3$ ) profiles and IR spectra of adsorbed pyridine (IR-Py) for acid molecular sieves with the AEL structure: (a) MAPO-11 sample; (b) SAPO-11 sample; (c) MAPSO-11(0.05) sample; (d) MAPSO-11(0.10) sample; (e) MAPSO-11(0.20) sample.

**Table 4** Concentrations of acid sites for molecular sieves with the AEL structure according to TPD-NH<sub>3</sub> data.

Sample	Acidity by NH <sub>3</sub> TPD, μmol/g				Acidity by IR-Py, μmol/g	
	Weak <sup>a</sup>	Moderate <sup>b</sup>	Strong <sup>c</sup>	Σ	BAS <sup>d</sup>	LAS <sup>d</sup>
MAPO-11(0.1MgO)	99	93	51	243	49	64
SAPO-11	185	145	23	353	91	19
MAPSO-11(0.05)	327	220	83	630	106	28
MAPSO-11(0.1)	295	205	103	603	109	40
MAPSO-11(0.2)	219	190	97	506	99	63

<sup>a</sup> The amount of ammonia desorbed in the range of 100-250 °C.

<sup>b</sup> The amount of ammonia desorbed in the range of 250-400 °C.

<sup>c</sup> The amount of ammonia desorbed in the range of 400-600 °C.

<sup>d</sup> BAS is the Brønsted acid sites and LAS is the Lewis acid sites.

These findings corroborate the NH<sub>3</sub>-TPD data and confirm that isomorphous substitution of phosphorus by silicon predominantly generates Brønsted sites, whereas magnesium incorporation favors the formation of Lewis sites, likely due to the generation of framework defects or extra-framework magnesium species.

To evaluate the catalytic efficiency of the synthesized materials, Pt-containing (0.5 wt.%) catalysts based on acid molecular sieves were prepared by wetness impregnation with an H<sub>2</sub>PtCl<sub>6</sub> solution. Hydrogen chemisorption measurements revealed Pt dispersion values in a relatively narrow range of 25–31% across the catalyst series: 25% for Pt/MAPO-11, 26% for Pt/SAPO-11, 27% for Pt/MAPSO-11(0.05), 29% for Pt/MAPSO-11(0.1), and 31% for Pt/MAPSO-11(0.2). According to previous studies, a platinum content of 0.5 wt.% is sufficient to provide a high dehydrogenation-hydrogenation function, as a result of which the acid-catalyzed transformation of hydrocarbons on the support becomes the rate-limiting step of the hydroisomerization process [50].

Catalytic tests (Figure 8, Table 5) revealed that the primary reaction products consist of mono- and dimethyl-branched C<sub>16</sub> alkane isomers. The monomethyl fraction comprises a broad distribution of methylpentadecanes, specifically 2-, 3-, 4-, 5-, 6-, 7-, and 8-methylpentadecanes, along with 2- and 3-ethyltetradecanes. Additionally, a wide variety of dimethyltetradecane isomers are formed. Common trends were observed for all catalysts samples: with increasing temperature, the conversion of n-hexadecane increased, but the selectivity towards isomers decreased due to enhanced side reactions of hydrocracking. At low conversions, monomethyl-branched isomers dominate, consistent with pore mouth and key-lock selec-

tivity (PMKLS) that favors less bulky transition states at the AEL channel entrances [51]. As conversion increases, these primary monomethyl intermediates undergo secondary isomerization, leading to a progressive rise in dimethyltetradecane concentrations. The accumulation of multi-branched species shifts the free-energy minimum toward β-scission pathways, making hydrocracking kinetically dominant at maximum conversion and ultimately reducing isomer selectivity.

The most effective in the studied series proved to be the Pt/MAPSO-11(0.1) sample, which demonstrated the most activity and selectivity with a maximum isomer yield of about 82%. The unique catalytic properties of this sample are determined by three key factors: a high concentration of strong BAS, an optimal primary nanocrystal size (50–100 nm), and a developed secondary mesoporous structure. The hierarchical pore system facilitates the transport of bulky reactant and product molecules, critically reducing the residence time of branched carbocationic intermediates in the microporous channels, while the strong acid sites enable isomerization to proceed at reduced temperatures. Collectively, this effectively suppresses β-scission (hydrocracking) reactions, which lead to the formation of undesirable light hydrocarbons.

Pt/MAPSO-11(0.05), despite exhibiting a comparable nanocrystalline size (50–100 nm), yielded 78% isomers due to its lower acid site density, reduced specific surface area, and diminished mesopore volume. Pt/SAPO-11 displayed the lowest activity, a consequence of its minimal concentration of strong acid sites, yet maintained a relatively high maximum yield (80%) owing to favorable crystal dimensions (50–100 nm).

**Table 5** Results of n-C<sub>16</sub> hydroisomerization at 3.0 MPa, 290 °C, WHSV 2.0 h<sup>-1</sup>, and H<sub>2</sub>/n-C<sub>16</sub> = 10

	Pt/MAPO-11	Pt/SAPO-11	Pt/MAPSO-11 (0.05)	Pt/MAPSO-11(0.1)	Pt/MAPSO-11 (0.2)
Conversion, wt. %	89.6	62.8	92.5	97.4	98.3
S <sub>Σ</sub> <sup>a</sup> , %	78.8	93.2	86.7	84.6	78.2
SMB <sup>a</sup> , %	30.8	77.5	50.7	44.9	23.8
SMTB <sup>a</sup> , %	48.0	15.7	36.0	39.7	54.4
3-mC <sub>15</sub> , wt. %	5.7	13.2	8.9	8.0	4.4
2-mC <sub>15</sub> , wt. %	5.4	13.3	8.1	7.1	4.4
4-mC <sub>15</sub> , wt. %	5.7	9.9	8.2	7.5	4.5
5-mC <sub>15</sub> , wt. %	8.1	12.5	8.4	6.3	4.5
Σ6–8-mC <sub>15</sub> , wt. %	14.2	34.3	25.0	24.1	12.6
MTB-C <sub>16</sub> <sup>b</sup> , wt. %	60.9	16.8	41.5	47.0	69.6

<sup>a</sup> S<sub>Σ</sub>, S<sub>MBS</sub>, and S<sub>MTB</sub> correspond to the selectivity of total C<sub>16</sub>H<sub>34</sub> isomers, monobranched C<sub>16</sub>H<sub>34</sub> isomers, and multibranched C<sub>16</sub>H<sub>34</sub> isomers respectively

<sup>b</sup> MTB-C<sub>16</sub> denotes the multi-branched i-C<sub>16</sub> isomers.

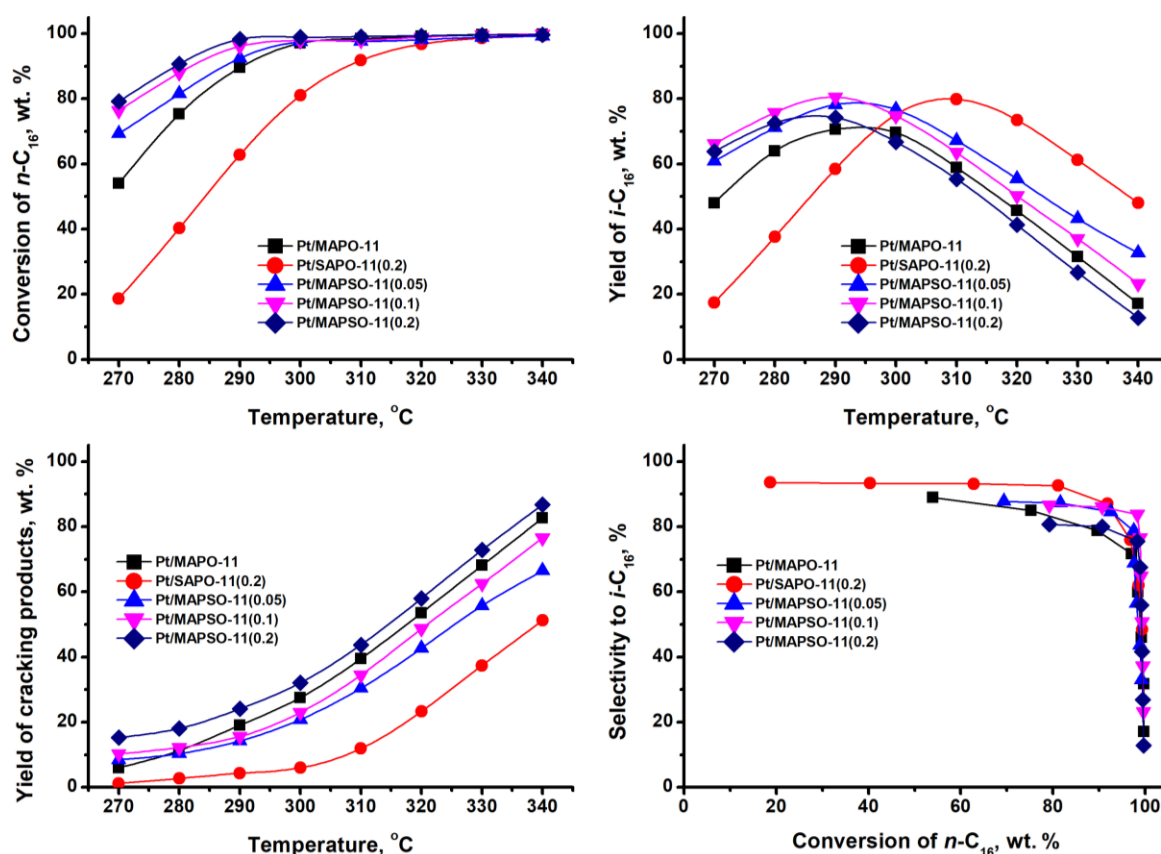


Figure 8. Results of n-hexadecane hydroisomerization over Pt-containing molecular sieve samples with the AEL structure.

Table 6 Catalytic performance comparison of different catalysts in hydroisomerization of n-hexadecane.

Catalyst	Conditions	n-C <sub>16</sub> conversion, %	i-C <sub>16</sub> yield, %	Ref.
Pt/MAPO-11(0.1)	290 °C, 2.0 h <sup>-1</sup> , 3.0 MPa, H <sub>2</sub> /n-C <sub>16</sub> molar ratio of 10	97	82	This work
Pt/SAPO-11-S1	340 °C, 8 h <sup>-1</sup> , 2 MPa	90	87	[52]
Pt/SAPO-11	340 °C, 1.0h <sup>-1</sup> , 1.5 MPa H <sub>2</sub> /n-C <sub>16</sub> volume ratio of 1000	82	71	[53]
Pt/SAPO-11-S	295 °C, 1.0 h <sup>-1</sup> , 6 MPa, H <sub>2</sub> /n-C <sub>16</sub> molar ratio of 15	86	80	[54]
Pt (EG)/SAPO-11	300 °C, H <sub>2</sub> /n-C <sub>16</sub> molar ratio of 44	35	33	[55]

Conversely, Pt/MAPO-11, characterized by significantly larger primary crystals (100–500 nm) and a moderate acid site concentration, showed intermediate activity but the lowest maximum isomer yield (70%), as diffusion limitations promote hydrocracking.

The sample with an excessive magnesium content, Pt/MAPO-11(0.2), exhibited a noticeable decrease in both activity and selectivity. As was shown in the sections devoted to physicochemical properties, this is explained by the formation of the largest primary crystals (100–200 nm) and a decrease in the overall crystallinity degree of the framework, which weakens the molecular sieving effect.

Furthermore, the coarsening of crystals to microcrystalline dimensions inevitably enhances diffusion limitations, which proportionally increases the contact time of molecules with the acid sites and stimulates the occurrence of side hydrocracking reactions. The maximum iso-C<sub>16</sub> yield achieved over the Pt/MAPO-11(0.1) catalyst is close to, and in some cases exceeds, the values reported in the literature for analogous bifunctional systems (Table 6), while being obtained at a relatively lower reaction temperature (290 °C).

### 3. Materials and methods

#### 3.1. Synthesis of molecular sieves with the AEL structure

Molecular sieves of the AEL structure type were synthesized by hydrothermal crystallization. The molar composition of the initial gel corresponded to the following ratio: 1.0Al<sub>2</sub>O<sub>3</sub>: 1.0P<sub>2</sub>O<sub>5</sub>:xMgO:ySiO<sub>2</sub>:1.0DPA:40H<sub>2</sub>O, where the parameter x was varied at 0.05, 0.1, or 0.2, and y was set to 0.2 for the silicon-containing systems. The following precursors were employed: orthophosphoric acid (H<sub>3</sub>PO<sub>4</sub>, 85%, Reakhim) as the phosphorus source, aluminum isopropoxide (Al(OPr)<sub>3</sub>, 98%, Acros Organics) as the aluminum source, and diisopropylamine (DIPA, C<sub>6</sub>H<sub>15</sub>N, 99%, Acros Organics) serving as the structure-directing agent (template). Silicon was introduced into the system in the form of a silica sol (SiO<sub>2</sub>), which was preliminarily prepared by the sol-gel method and characterized by an average particle size of approximately 3 nm [56]. The source of magnesium was magnesium nitrate hexahydrate (Mg(NO<sub>3</sub>)<sub>2</sub>\*6H<sub>2</sub>O, 99%, Acros Organics).

A typical synthesis procedure included the following steps. At the first stage, 10.0 g of orthophosphoric acid was diluted with 15.0 g of distilled water, after which 4.4 g of diisopropylamine was introduced into the solution under intensive stirring, maintaining the homogenization of the suspension for 1 h. Then, 17.7 g of aluminum isopropoxide was added portionwise to the resulting mixture, with continuous stirring maintained. Upon achieving homogeneity of the aluminophosphate gel, calculated amounts of silicon and/or magnesium precursors were introduced into the reaction medium, depending on the desired composition of the target product. The mixture was additionally stirred for 1 h and then subjected to preliminary aging at a temperature of 50 °C for 24 h. This stage was critically important for suppressing the formation of the concomitant non-porous tridymite phase. The gel prepared in this manner was transferred into a steel autoclave equipped with a Teflon liner, where hydrothermal crystallization was carried out at 200 °C for 24 h.

Upon completion of the crystallization process, the autoclave was cooled to room temperature. The formed solid product was separated by centrifugation and subjected to repeated washing with distilled water until the washings reached a neutral pH. The purified precipitate was dried at 90 °C for 24 h. Depending on the chemical composition of the initial gel, the synthesized materials were classified as MAPO-11, SAPO-11, and a series of MAPSO-11(x), where the value in parentheses reflects the specified MgO/Al<sub>2</sub>O<sub>3</sub> molar ratio in the reaction mixture.

### 3.2. Physicochemical characterization methods

The chemical composition of the reaction gels and synthesized materials was determined by X-ray fluorescence analysis (XRF) using a Shimadzu EDX-7000P spectrometer with the fundamental parameters method.

The phase composition of uncalcined samples was investigated by X-ray diffraction (XRD) on a Shimadzu XRD-7000 powder diffractometer using CuK $\alpha$  radiation ( $\lambda = 1.5406 \text{ \AA}$ ). Diffraction patterns were recorded in the  $2\theta$  angle range from 5° to 40° with a scanning rate of 1°/min. Identification of crystalline phases was performed by comparing the obtained data with the PDF-2 database. The crystallinity degree of the samples was assessed using Shimadzu XRD Crystallinity software as the ratio of the total integral intensity of the characteristic diffraction peaks to the intensity of the amorphous halo in the angular range of 20–30° on the  $2\theta$  scale.

Morphology and crystal sizes were studied using scanning electron microscopy (SEM) on a Hitachi Regulus SU8220 field-emission electron microscope. Image registration was performed in secondary electron detection mode at an accelerating voltage of 2 kV.

For a more detailed analysis of the microstructure (using the SAPO-11 system as an example), transmission electron microscopy (TEM) and high-resolution TEM (HRTEM) were employed. The investigations were carried out on

Hitachi HT7700 (accelerating voltage 100 kV) and Thermo Fisher Scientific ThemisZ (200 kV) microscopes. The interplanar spacings were calculated based on the analysis of micrographs using the Fast Fourier Transform (FFT) algorithm.

The local coordination environment of silicon atoms was investigated by magic angle spinning nuclear magnetic resonance spectroscopy on <sup>29</sup>Si nuclei (<sup>29</sup>Si MAS NMR). The spectra were recorded on a Bruker Avance-400 spectrometer (magnetic field induction 9.4 T) at a resonance frequency of 79.49 MHz using a 4-mm H/X MAS probe. To enhance the sensitivity of the method, cross-polarization (CP/MAS) was employed with a RAMP pulse sequence (amplitude variation on protons from 70 to 100%) at a contact time of 3 ms. Heteronuclear dipole-dipole interactions were suppressed using SW-TPPM proton decoupling. The duration of the 90° radiofrequency pulse for <sup>1</sup>H was 2.5  $\mu$ s, and the relaxation delay was 10 s. Spectra were obtained by accumulating from 8000 to 13000 free induction decays at a rotor spinning rate of 8 kHz. The chemical shift scale was calibrated with respect to an external standard – tetramethylsilane (0 ppm). Deconvolution of complex spectral contours was performed using the Dmfit software package.

Textural characteristics of the porous materials were determined by low-temperature (77 K) physical adsorption of nitrogen using an Altamira Instruments QUICK-200 automatic analyzer. Preliminarily, the samples were subjected to oxidative thermal treatment in air at 600 °C for 6 h. The specific surface area was calculated by the multipoint Brunauer–Emmett–Teller (BET) method. The micropore volume was estimated using the t-plot method, while the mesopore size distribution was calculated within the framework of the Barrett–Joyner–Halenda (BJH) model based on the desorption branch of the isotherm.

The acidic properties of the catalysts were studied in detail by temperature-programmed desorption of ammonia (TPD-NH<sub>3</sub>) and infrared spectroscopy of adsorbed pyridine. The total acidity and the distribution of acid sites by strength were evaluated using TPD-NH<sub>3</sub> on an Altamira AMI-400TPx chemisorption analyzer. Before analysis, the samples were calcined in a helium flow at 600 °C for 4 h. Saturation of the surface with ammonia was carried out from a gas mixture (10 vol.% NH<sub>3</sub> in He) at 100 °C for 30 min, followed by purging with pure helium at the same temperature to remove physically adsorbed molecules. Desorption was recorded with a thermal conductivity detector in the temperature range from 100 to 600 °C at a linear heating rate of 10 °C/min.

Quantitative differentiation of Brønsted (BAS) and Lewis (LAS) acid sites was performed using a Bruker Vertex-70V FTIR spectrometer equipped with a DTGS detector in the spectral range of 4000–400 cm<sup>-1</sup> with an optical resolution of 4 cm<sup>-1</sup>. Samples, pressed into self-supporting wafers (diameter 20 mm, mass 15–20 mg), were placed in a specialized vacuum thermal cell with CaF<sub>2</sub> windows and

evacuated under vacuum ( $10^{-3}$  mbar) at 450 °C for 1 h. Adsorption of pyridine vapor was carried out at 150 °C for 30 minutes, after which the excess reagent was evacuated at the same temperature for 30 minutes. The concentrations of BAS and LAS were calculated by integrating the areas of the characteristic absorption bands corresponding to the pyridinium ion ( $\text{PyH}^+$ ,  $\sim 1545\text{ cm}^{-1}$ ) and coordinative-bound pyridine ( $\text{PyL}$ ,  $\sim 1449\text{--}1454\text{ cm}^{-1}$ ), using standardized molar extinction coefficients [49].

Additionally, to evaluate the platinum dispersion and the average size of metal particles in the pre-reduced catalysts, pulse hydrogen chemisorption was performed on an Altamira AMI-400TPx setup, assuming an adsorption stoichiometry of  $\text{H}/\text{Pt} = 1$ .

### 3.3. Preparation and characterization of bifunctional catalysts

To form bifunctional catalytic systems based on acid molecular sieves with the AEL structure, the synthesized supports were preliminarily subjected to oxidative thermal treatment in air at 600 °C for 6 h. Introduction of the metallic function to obtain catalysts with a composition of 0.5 wt.% Pt/SAPO-11 was carried out by incipient wetness impregnation of the support. An aqueous solution of chloroplatinic acid ( $\text{H}_2\text{PtCl}_6 \cdot 6\text{H}_2\text{O}$ ) was used as the precursor of the active component. Upon completion of impregnation, the wet samples were dried at 100 °C for 24 h, followed by calcination in an air flow at 550 °C for 5 h for complete thermal decomposition of the platinum complex. The final stage of preparation consisted of catalyst activation, which was performed by their reduction in a dynamic hydrogen flow at 400 °C for 5 h immediately prior to the start of catalytic testing.

### 3.4. Catalytic testing in the n-hexadecane hydroisomerization reaction

The catalytic properties of the synthesized bifunctional systems were studied in the model reaction of n-hexadecane ( $\text{C}_{16}\text{H}_{34}$ , 98%) hydroisomerization. The process was carried out in a flow catalytic unit with a fixed catalyst bed in a stainless steel reactor at an operating pressure of 3.0 MPa. The tests were conducted in the temperature range from 270 to 340 °C. The flow rate of hexadecane was 0.1 ml/min. During the experiments, a constant hydrogen-to-hydrocarbon molar ratio ( $\text{H}_2/\text{C}_{16}\text{H}_{34}$ ) of 10 was maintained, while the weight hourly space velocity (WHSV) of the feed was  $2\text{ h}^{-1}$ . Prior to data acquisition at each temperature, the system was allowed to stabilize for 3 h to ensure steady-state conditions. Steady state was confirmed when the variation in n-hexadecane conversion was within  $\pm 1\%$  over two consecutive analyses (interval: 30 min).

The analysis of the liquid reaction mixture composition was performed using a Chromatek-Crystal 5000 gas chromatograph equipped with a flame ionization detector (FID) and a capillary column (50 m  $\times$  0.2 mm) containing

cross-linked dimethylpolysiloxane as the stationary phase. Gaseous products were analyzed using a Meta-Chrom Crystallux-4000M chromatograph equipped with a thermal conductivity detector and a capillary column (50 m  $\times$  0.32 mm) with a  $\text{Al}_2\text{O}_3/\text{KCl}$  phase. The main catalytic performance indicators, including the total conversion of n-hexadecane, the selectivity towards target products, and the yield of isomeric hydrocarbons, were quantitatively calculated based on the mathematical processing of the areas of the corresponding chromatographic peaks.

## 4. Limitations

This section outlines encountered difficulties and potential solutions. Despite successfully developing a template-free synthesis for hierarchical MAPSO-11 molecular sieves, several limitations remain:

- Incomplete Heteroatom incorporation and crystallinity Loss: Magnesium and silicon incorporation into the framework is incomplete due to kinetic and thermodynamic limitations. Moreover, increasing the initial  $\text{MgO}/\text{Al}_2\text{O}_3$  ratio to 0.2 causes lattice distortions, partial amorphization (crystallinity drops to 85%), and decreased catalytic performance due to crystal coarsening. Possible Solution: future studies should fine-tune hydrothermal crystallization parameters (e.g., pH, time, temperature) or explore alternative precursors to maximize incorporation efficiency while preserving structural integrity and nanoscale morphology.

- Dependence on specific precursors: forming the hierarchical micro-mesoporous structure heavily relies on highly reactive aluminum isopropoxide and a specific nanosized  $\text{SiO}_2$  sol ( $\sim 3\text{ nm}$ ). While avoiding costly organic templates, procuring these precursors might present economic and logistical challenges for large-scale industrial manufacturing. Possible solution: future research could evaluate substituting these chemicals with more cost-effective, commercially available alternatives that maintain crystal growth inhibition, or optimize the sol-gel preparation step for easier scaling.

- Use of a model reaction feedstock: Catalytic efficiency was evaluated using pure n-hexadecane. While providing fundamental insights into hydroisomerization, real industrial feedstocks for isodewaxing contain complex heavy hydrocarbon mixtures and potential catalytic poisons (e.g., sulfur or nitrogen compounds). Possible Solution: To facilitate industrial implementation, future testing should use real petroleum feedstocks under industrially relevant conditions to comprehensively assess the catalyst's long-term stability, deactivation rates, and regenerability.

## 5. Conclusions

In the present work, an efficient and environmentally benign method for the hydrothermal synthesis of hierarchical bifunctional Pt/MAPSO-11 molecular sieves with the

AEL structure type has been proposed. An important advantage of this approach is the complete avoidance of expensive secondary pore-forming templates and organic crystal growth modifiers, which significantly reduces the environmental burden of the process.

Based on a comprehensive set of physicochemical characterization methods, it has been established that the use of a highly reactive aluminum precursor (isopropoxide) in combination with nanosized SiO<sub>2</sub> sol acts as a key factor in inhibiting crystal growth. This enables the formation of primary MAPSO-11 nanocrystals of 50–100 nm in size (in the form of plates and cubes) with developed intercrystalline mesoporosity. As a result, the effective length of the one-dimensional 10-membered ring diffusion channels is reduced by a factor of 5–10 compared to conventional microcrystalline samples, which radically improves the transport characteristics of the synthesized material.

Furthermore, along with targeted morphological control, the isomorphous substitution of framework atoms by magnesium and silicon exerts a synergistic effect on the acidic properties. While silicon generates predominantly acid sites of moderate strength, the introduction of magnesium (up to the attainment of the optimal MgO/Al<sub>2</sub>O<sub>3</sub> molar ratio of 0.1) leads to the formation of a high concentration of strong Brønsted acid sites.

Catalytic testing of the synthesized materials in the model reaction of n-hexadecane hydroisomerization fully confirmed the effectiveness of the proposed approach. The best performance was demonstrated by the Pt/MAPSO-11(0.1) bifunctional catalyst, which enabled achieving a maximum yield of target C<sub>16</sub> isomers of approximately 82% at a reduced temperature (290 °C).

Such high catalytic efficiency is due to a comprehensive synergistic effect. Strong Brønsted acid sites ensure that the isomerization reaction proceeds at lower temperatures, reducing energy consumption, while the hierarchical nanocrystalline structure minimizes intradiffusion limitations. The reduced residence time of bulky branched intermediates within the pore system effectively prevents the occurrence of secondary side hydrocracking reactions. Thus, the developed approach to the synthesis of nanosized Pt/MAPSO-11 represents a promising strategy for the design of highly efficient and selective industrial catalysts for isodewaxing processes aimed at producing low-pour-point winter fuels and oils.

### Supplementary materials

No supplementary materials are available.

### Data availability statement

The data that support the findings of this study are available on request from the corresponding author

### Acknowledgments

This research was funded by the Russian Science Foundation No. 23-73-10153.

### Author contributions

Conceptualization: M. A.  
 Data curation: M. A.  
 Formal Analysis: D. S., N.F.  
 Funding acquisition: M.A.  
 Investigation: D.S., A.M., N.F., S.K., A.B.  
 Methodology: M.A., R.Y.  
 Project administration: M.A.  
 Resources: M.A.  
 Software: D.S., A.M., N.F.,  
 Supervision: M.A., D.S.  
 Validation: M.A., D.S., N.F.  
 Visualization: N.F.  
 Writing – original draft: D.S., N.F.  
 Writing – review & editing: M.A., D.S., N.F.

### Conflict of interest

The authors declare no conflict of interest.

### Additional information

Author Scopus IDs:

Artur Malunov: [58772198900](https://orcid.org/58772198900);  
 Dmitry Serebrennikov: [57210346068](https://orcid.org/57210346068);  
 Roman Yakovenko: [49061667800](https://orcid.org/49061667800);  
 Nadezhda Filippova: [57023467900](https://orcid.org/57023467900);  
 Svetlana Kostyleva: [55734844700](https://orcid.org/55734844700);  
 Marat Agliullin: [56480769400](https://orcid.org/56480769400).

Websites:

Institute of Catalysis and Petrochemistry: <http://ipc-ras.ru/ru>;  
 Platov South-Russian State Polytechnic University (NPI):  
<https://www.npi-tu.ru>;  
 Ufa Federal Research Center of the Russian Academy of Sciences: <http://www.ufaras.ru>.

### References

- Martínez C, Corma A. Inorganic molecular sieves: Preparation, modification and industrial application in catalytic processes. *Coordination Chemistry Reviews*. 2011;255:1558–80. doi:10.1016/j.ccr.2011.03.014.
- Pérez-Botella E, Valencia S, Rey F. Zeolites in Adsorption Processes: State of the Art and Future Prospects. *Chem Rev*. 2022;122:17647–95. doi:10.1021/acs.chemrev.2c00140.
- Potter ME. Down the Microporous Rabbit Hole of Silicoaluminophosphates: Recent Developments on Synthesis, Characterization, and Catalytic Applications. *ACS Catal*. 2020;10:9758–89. doi:10.1021/acscatal.0c02278.
- Hartmann M, Elangovan SP. Catalysis with Microporous Aluminophosphates and Silicoaluminophosphates Containing Transition Metals. *Advances in Nanoporous Materials*, vol. 1, Elsevier; 2010, p. 237–312. doi:10.1016/S1878-7959(09)00104-2.
- Yadav R, Singh AK. Recent Developments on Clean Fuels over SAPO-Type Catalysts. In: Pant KK, Gupta SK, Ahmad E, editors. *Catalysis for Clean Energy and Environmental Sustainability*, Cham: Springer International Publishing; 2021, p. 503–25. doi:10.1007/978-3-030-65021-6\_16.
- Du Y, Wright PA. Aluminophosphate Zeotypes: Structural Chemistry and Applications. In: Serrano DP, Čejka J, editors. *Zeolites*, Royal Society of Chemistry; 2025, p. 155–96. doi:10.1039/9781837676859-00155.
- Baerlocher C, McCusker LB, Olson DH. *Atlas of Zeolite Framework Types*. Elsevier. 2007.
- Wang Q, Zhang W, Ma X, Liu Y, Zhang L, Zheng J, et al. A highly efficient SAPO-34 catalyst for improving light olefins in methanol conversion: Insight into the role of hierarchical porosities and tailoring acid properties based on in situ NH<sub>3</sub>-poisoning. *Fuel*. 2023;331:125935. doi:10.1016/j.fuel.2022.125935.

9. Aljajan Y, Stytsenko V, Rubtsova M, Glotov A. Hydroisomerization Catalysts for High-Quality Diesel Fuel Production. *Catalysts*. 2023;13:1363. doi:10.3390/catal13101363.
10. Serebrennikov DV, Filippova NA, Fayzullina ZR, Mescheryakova ES, Kutepov BI, Sabirov DSh, et al. Hydroisomerization of n-Hexadecane over Pt/SAPO-11 and Pt/SAPO-41 Molecular Sieves Differing in Crystal Morphology and Size. *Pet Chem*. 2025;65:369–77. doi:10.1134/S096554412560081X.
11. Miller SJ. New molecular sieve process for lube dewaxing by wax isomerization. *Microporous Materials*. 1994;2:439–49. doi:10.1016/0927-6513(94)00016-6.
12. Yu G, Qiu M, Wang T, Ge L, Chen X, Wei W. Optimization of the pore structure and acidity of SAPO-11 for highly efficient hydroisomerization on the long-chain alkane. *Microporous and Mesoporous Materials*. 2021;320:111076. doi:10.1016/j.micromeso.2021.111076.
13. Yadav R, Sakthivel A. Silicoaluminophosphate molecular sieves as potential catalysts for hydroisomerization of alkanes and alkenes. *Applied Catalysis A: General*. 2014;481:143–60. doi:10.1016/j.apcata.2014.05.010.
14. Torres-Bujalance V, Prieto CA, Rodriguez Espinoza KE, González-Mendoza LA. Production of Biofuels from Hydrodeoxygenation and Hydroisomerization of Triglycerides with Metal-Supported SAPO-11 Molecular Sieves. *Energy Fuels* 2024;38:4312–4324. doi:10.1021/acs.energyfuels.3c04992.
15. Tuo C, Liu Q, Wu X, Abulizi A, Ren T, Nulhong A. Preparation and n-hexadecane hydroisomerization properties of SAPO-11-based composite molecular sieve. *Res Chem Intermed* 2024;50:5491–5523. doi:10.1007/s11164-024-05393-4.
16. Jang JH, Kim HJ, Kim JH, Lee JE, Jang HS, Kang SH. Evaluation of Waste-Plastic Pyrolysis Oil as a Potential Feedstock for Lubricant Base Oil Production via Hydroprocessing. *Sustainability* 2026;18:2655. doi:10.3390/su18052655.
17. Zheng D, Li L, Yu S. In-situ synthesis of NiMo@SAPO-11 under mild conditions for the hydrodeoxygenation of triolein. *Molecular Catalysis* 2025;579:115076. doi:10.1016/j.mcat.2025.115076.
18. Li X, Fan Q, Wu K, Liu N, Zhang W, Liu Y, et al. Enhancing catalytic isomerization ability of SAPO-11 by typical acid modification in preparation of green diesel by one-step hydrotreatment of FAME. *Renewable Energy* 2024;224:120226. doi:10.1016/j.renene.2024.120226.
19. Zhang M, Long H, Fan D, Wang L, Wang Q, Chen Y, et al. Synthesis of ZSM-48 zeolites and their catalytic performance: a review. *Catal Sci Technol*. 2022;12:5097–109. doi:10.1039/D2CY00267A.
20. Parfenov MV, Pirutko LV, Yakovlev IV, Lapina OB, Prosvirin IP, Klimov OV, et al. Role of Zeolite Acidity and Ni Content in Hexadecane Hydroisomerization over Ni/ZSM-23 Catalyst. *Ind Eng Chem Res*. 2024;63:5557–72. doi:10.1021/acs.iecr.3c03574.
21. Bensafi B, Chouat N, Djafri F. The universal zeolite ZSM-5: Structure and synthesis strategies. A review. *Coordination Chemistry Reviews*. 2023;496:215397. doi:10.1016/j.ccr.2023.215397.
22. Gianotti E, Manzoli M, Potter ME, Shetti VN, Sun D, Paterson J, et al. Rationalising the role of solid-acid sites in the design of versatile single-site heterogeneous catalysts for targeted acid-catalysed transformations. *Chem Sci*. 2014;5:1810–9. doi:10.1039/C3SC53088D.
23. Elangovan SP, Hartmann M. Evaluation of Pt/MCM-41/MgAPO-n composite catalysts for isomerization and hydrocracking of n-decane. *Journal of Catalysis*. 2003;217:388–95. doi:10.1016/S0021-9517(03)00042-3.
24. Yang X, Xu Z, Tian Z, Ma H, Xu Y, Qu W, et al. Performance of Pt/MgAPO-11 Catalysts in the Hydroisomerization of n-dodecane. *Catal Lett*. 2006;109:139–45. doi:10.1007/s10562-006-0070-6.
25. Agliullin MR, Kutepov BI, Ostroumova VA, Maximov AL. Silicoaluminophosphate Molecular Sieves SAPO-11 and SAPO-41: Synthesis, Properties, and Applications for Hydroisomerization of C16+ n-Paraffins. Part 2: Current State of Research on Methods to Control the Crystal Morphology, Dispersion, Acidic Properties, Secondary Porous Structure, and Catalytic Properties of SAPO-11 and SAPO-41 in Hydroisomerization of C16+ n-Paraffins (A Review). *Pet Chem*. 2021;61:852–70. doi:10.1134/S096554412108003X.
26. Agliullin MR, Kutepov BI, Ostroumova VA, Maximov AL. Silicoaluminophosphate Molecular Sieves SAPO-11 and SAPO-41: Synthesis, Properties, and Applications for Hydroisomerization of C16+ n-Paraffins. Part 1: Current State of Research on SAPO-11 and SAPO-41 Synthesis (A Review). *Pet Chem*. 2021;61:836–51. doi:10.1134/S0965544121080028.
27. Wang P, Liu H, Wang C, Lv G, Wang D, Ma H, et al. Direct synthesis of shaped MgAPO-11 molecular sieves and the catalytic performance in n-dodecane hydroisomerization. *RSC Adv* 2021;11:25364–74. doi:10.1039/D1RA03758G.
28. Tao S, Li X, Gong H, Jiang Q, Yu W, Ma H, et al. Confined-space synthesis of hierarchical MgAPO-11 molecular sieves with good hydroisomerization performance. *Microporous and Mesoporous Materials* 2018;262:182–90. doi:10.1016/j.micromeso.2017.11.041.
29. Chen Z, Song W, Zhu S, Lai W, Yi X, Fang W. Synthesis of a multi-branched dandelion-like SAPO-11 by an in situ inoculating seed-induced-steam-assisted conversion method (SISAC) as a highly effective hydroisomerization support. *RSC Adv*. 2017;7:4656–66. doi:10.1039/c6ra26522g.
30. Chen Z, Li X, Xu Y, Dong Y, Lai W, Fang W, et al. Fabrication of nano-sized SAPO-11 crystals with enhanced dehydration of methanol to dimethyl ether. *Catalysis Communications*. 2018;103:1–4. doi:10.1016/j.catcom.2017.09.002.
31. Jin D, Ye G, Zheng J, Yang W, Zhu K, Coppens M-O, et al. Hierarchical Silicoaluminophosphate Catalysts with Enhanced Hydroisomerization Selectivity by Directing the Orientated Assembly of Premanufactured Building Blocks. *ACS Catal*. 2017;7:5887–902. doi:10.1021/acscatal.7b01646.
32. Jin D, Li L, Ye G, Ding H, Zhao X, Zhu K, et al. Manipulating the mesostructure of silicoaluminophosphate SAPO-11 tumbling-assisted, oriented assembly crystallization: a pathway to enhance selectivity in hydroisomerization. *Catal Sci Technol*. 2018;8:5044–61. doi:10.1039/c8cy01483c.
33. Guo L, Bao X, Fan Y, Shi G, Liu H, Bai D. Impact of cationic surfactant chain length during SAPO-11 molecular sieve synthesis on structure, acidity, and n-octane isomerization to dimethyl hexanes. *Journal of Catalysis*. 2012;294:161–70. doi:10.1016/j.jcat.2012.07.016.
34. Chen B, Huang Y. Examining the Self-Assembly of Microporous Material AlPO<sub>4</sub>-11 by Dry-Gel Conversion. *J Phys Chem C*. 2007;111:15236–43. doi:10.1021/jp071868f.
35. Agliullin MR, Serebrennikov DV, Kutepov BI. Changing Template/Al<sub>2</sub>O<sub>3</sub> Ratio in Reaction Gel—An Effective Way to Regulate Nature of Intermediate Phases and Properties of SAPO-11 Molecular Sieves during Crystallization. *Materials*. 2024;17:1359. doi:10.3390/ma17061359.
36. Agliullin MR, Shamanaeva IA, Zabirov AR, Lazarev VV, Maistrenko VN, Kutepov BI. Influence of the Nature of the Al Source on the Properties of the Initial Reaction Gels for Crystallization of Molecular Sieve AlPO<sub>4</sub>-11. *Pet Chem*. 2022;62:291–300. doi:10.1134/S096554412203001X.
37. Agliullin MR, Kolyagin YG, Serebrennikov DV, Grigor'eva NG, Dmitrenok AS, Maistrenko VN, et al. Acid properties and morphology of SAPO-11 molecular sieve controlled by silica source. *Microporous and Mesoporous Materials*. 2022;338:111962. doi:10.1016/j.micromeso.2022.111962.
38. Elanany M, Vercauteren DP, Kubo M, Miyamoto A. The acidic properties of H-MeAlPO-5 (Me=Si, Ti, or Zr): A periodic density functional study. *Journal of Molecular Catalysis A: Chemical*. 2006;248:181–4. doi:10.1016/j.molcata.2005.12.026.
39. Mortén M, Cordero-Lanzac T, Cnudde P, Redekop EA, Svelle S, Van Speybroeck V, et al. Acidity effect on benzene methylation kinetics over substituted H-MeAlPO-5 catalysts. *Journal of Catalysis*. 2021;404:594–606. doi:10.1016/j.jcat.2021.11.002.

40. Su B, Sanchez C, Yang X. Hierarchically Structured Porous Materials: From Nanoscience to Catalysis, Separation, Optics, Energy, and Life Science. 1st ed. Wiley; 2011. [doi:10.1002/9783527639588](https://doi.org/10.1002/9783527639588).
41. Cejka J, Bekkum H van, Corma A, Schueth F. Introduction to Zeolite Molecular Sieves. Elsevier; 2007.
42. Kurttepel M, Locus R, Verboekend D, De Clippel F, Breynaert E, Martens J, et al. Synthesis of aluminum-containing hierarchical mesoporous materials with columnar mesopore ordering by evaporation induced self-assembly. *Microporous and Mesoporous Materials*. 2016;234:186–95. [doi:10.1016/j.micromeso.2016.07.002](https://doi.org/10.1016/j.micromeso.2016.07.002).
43. Wang H-Q, Cui Y-Q, Ding Y-L, Xiang M, Yu P, Li R-Q. Synthesis of Hierarchical Porous SAPO-34 and Its Catalytic Activity for 4,6-Dimethyldibenzothiophene. *Front Chem*. 2022;10:854664. [doi:10.3389/fchem.2022.854664](https://doi.org/10.3389/fchem.2022.854664).
44. Barthomeuf D. Topological model for the compared acidity of SAPOs and SiAl zeolites. *Zeolites*. 1994;14:394–401. [doi:10.1016/0144-2449\(94\)90164-3](https://doi.org/10.1016/0144-2449(94)90164-3).
45. Zhang L, Huang Y. Crystallization and catalytic properties of molecular sieve SAPO-34 by a vapor-phase transport method. *J Mater Chem A*. 2015;3:4522–9. [doi:10.1039/C4TA06775D](https://doi.org/10.1039/C4TA06775D).
46. Liu P, Ren J, Sun Y. Influence of template on Si distribution of SAPO-11 and their performance for n-paraffin isomerization. *Microporous and Mesoporous Materials*. 2008;114:365–72. [doi:10.1016/j.micromeso.2008.01.022](https://doi.org/10.1016/j.micromeso.2008.01.022).
47. Greiser S, Gluth GJG, Sturm P, Jäger C.  $^{29}\text{Si}\{^{27}\text{Al}\}$ ,  $^{27}\text{Al}\{^{29}\text{Si}\}$  and  $^{27}\text{Al}\{^1\text{H}\}$  double-resonance NMR spectroscopy study of cementitious sodium aluminosilicate gels (geopolymers) and gel-zeolite composites. *RSC Adv*. 2018;8:40164–71. [doi:10.1039/C8RA09246J](https://doi.org/10.1039/C8RA09246J).
48. Corà F, Catlow CRA, Civalleri B, Orlando R. Acid Strength of Low-Valence Dopant Ions in Microporous Zeolites and AlPOs. *J Phys Chem B*. 2003;107:11866–70. [doi:10.1021/jp035553l](https://doi.org/10.1021/jp035553l).
49. Tamura M, Shimizu K, Satsuma A. Comprehensive IR study on acid/base properties of metal oxides. *Applied Catalysis A: General*. 2012;433–434:135–45. [doi:10.1016/j.apcata.2012.05.008](https://doi.org/10.1016/j.apcata.2012.05.008).
50. Yu R, Tan Y, Yao H, Xu Y, Huang J, Zhao B, et al. Toward n-Alkane Hydroisomerization Reactions: High-Performance Pt-Al<sub>2</sub>O<sub>3</sub>/SAPO-11 Single-Atom Catalysts with Nanoscale Separated Metal-Acid Centers and Ultralow Platinum Content. *ACS Appl Mater Interfaces*. 2022;14:44377–88. [doi:10.1021/acsami.2c11607](https://doi.org/10.1021/acsami.2c11607).
51. Akhmedov VM, Al-Khowaiter SH. Recent Advances and Future Aspects in the Selective Isomerization of High n-Alkanes. *Catalysis Reviews* 2007;49:33–139. [doi:10.1080/01614940601128427](https://doi.org/10.1080/01614940601128427).
52. Mu C, Sun J, Xie C, Xu J, Bao J, Zhang H, et al. Bio-fuel production from hydroconversion of hexadecane over Pt/SAPO-11 catalysts. *Fuel* 2024;369:131732. [doi:10.1016/j.fuel.2024.131732](https://doi.org/10.1016/j.fuel.2024.131732).
53. Yang S, Liu X, Zhang X, Sun W, Ma Q, Song N, et al. Isomerization Properties of Pt/SAPO-11 Catalysts for the Production of Bio-Aviation Kerosene. *Catalysts* 2023;13:1100. [doi:10.3390/catal13071100](https://doi.org/10.3390/catal13071100).
54. Du Y, Feng B, Jiang Y, Yuan L, Huang K, Li J. Solvent-Free Synthesis and n-Hexadecane Hydroisomerization Performance of SAPO-11. *Eur J Inorg Chem* 2018;2018:2599–606. [doi:10.1002/ejic.201800134](https://doi.org/10.1002/ejic.201800134).
55. Said S, Zaky MT. Pt/SAPO-11 Catalysts: Effect of Platinum Loading Method on the Hydroisomerization of n-Hexadecane. *Catal Lett* 2019;149:2119–31. [doi:10.1007/s10562-019-02783-x](https://doi.org/10.1007/s10562-019-02783-x).
56. Agliullin MR, Serebrennikov DV, Gerasimov EYu, Larichev YV, Filippova NA, Zabirov AR, et al. Tailoring Silicoaluminophosphate SAPO-11 Nanocrystal Morphology: Silicon Content as a Switch for Two-Dimensional Growth and Enhanced Catalytic Performance in Isodewaxing of Gas-to-Liquid Waxes. *ACS Appl Nano Mater*. 2026;9:2771–88. [doi:10.1021/acsnanm.5c04997](https://doi.org/10.1021/acsnanm.5c04997).